International Journal of Nanomedicine

Dovepress
Taylor & Francis Group

Open Access Full Text Article

ORIGINAL RESEARCH

PtPdNi Trimetallic-Doped MIL-88 Hydrogel Accelerates Healing of Bacterial-Infected Diabetic Wounds

Yawen Peng[1,2,*], Wenjuan Du[3,*], Yating Cui[1,*], Chenri Su[4], Yuyu Liu[1], Yang Bai[2], Wen Li[1], Juan Zhang[2], Xianhua Wang[4], Shihui Fu[5,6], Haiyan Zhu[2]

[1]Medical School of Chinese PLA, Chinese PLA General Hospital, Beijing, 100853, People's Republic of China; [2]Department of Emergency, The First Medical Center of Chinese PLA General Hospital, Beijing, 100853, People's Republic of China; [3]Medical Innovation Research Department of PLA General Hospital, Beijing, 100853, People's Republic of China; [4]Tianjin Key Laboratory on Technologies Enabling Development of Clinical Therapeutics and Diagnostics, School of Pharmacy, Tianjin Medical University, Tianjin, 300070, People's Republic of China; [5]Department of Cardiology, Hainan Hospital of Chinese People's Liberation Army General Hospital, Sanya, 572013, People's Republic of China; [6]Department of Geriatric Cardiology, Chinese People's Liberation Army General Hospital, Beijing, 100853, People's Republic of China

*These authors contributed equally to this work

Correspondence: Haiyan Zhu, 28th Fuxing Road, Haidian District, Beijing, 100853, People's Republic of China, Email xiaoyanzibj301@163.com; Shihui Fu, 80th Jianglin Road, Haitang District, Sanya, 572013, People's Republic of China, Email xiaoxiao0915@126.com

Purpose: Treatment of bacterial-infected diabetic wounds is still challenging due to the susceptibility to bacterial infection and oxidative stress. Therefore, a novel multifunctional platform was established for accelerating the healing of bacterial-infected diabetic wounds.

Methods: PtPdNi trimetallic-doped MIL-88 (PPNM) was fabricated and anchored to polyvinyl alcohol/sodium alginate (PVA/SA) matrix for constructing PPNM-containing hydrogel (PPNM-Gel). The basic properties of PPNM were characterized by TEM, SEM, XPS, FT-IR spectra, and UV-vis spectra. Adhesive, swelling, and degradation properties of PPNM-Gel were also analyzed. In vitro biocompatibility of PPNM-Gel was determined using L929 and HUVEC-SV40 cells. In vitro antimicrobial effects of PPNM-Gel were evaluated with *E. coli* and *S. aureus*. In vivo antibacterial and wound healing evaluation of PPNM-Gel was performed in the STZ-induced diabetic SD rats, which were established by intraperitoneal injection of STZ, followed by full-thickness skin wound preparation and bacterial infection. Histological and immunofluorescence staining were used to evaluate the status of epithelization, collagen deposition and inflammation response.

Results: PPNM exhibited multienzyme-like activity including POD-like, OXD-like, CAT-like, SOD-like, and NAD-like activities. PPNM-Gel demonstrated excellent tissue adhesive activity, water absorption ability, biodegradability, and biocompatibility. In vitro testing, PPNM-Gel showed obvious antibacterial ability against *E. coli* and *S. aureus* in a PPNM dose-dependent approach, and its antibacterial ability against *E. coli* was stronger than that against *S. aureus*. In the STZ-induced diabetic SD rats, PPNM-Gel effectively accelerated wound remodeling by killing pathogenic bacteria, reducing inflammation, and promoting collagen deposition.

Conclusion: PPNM-Gel significantly accelerated the healing of bacterial-infected diabetic wounds in the rat model. Therefore, PPNM-Gel showed great promise for the treatment of diseases affected by bacterial infections and high ROS levels.

Keywords: trimetallic nanozyme, multienzyme-like activity, hydrogel, bacterial-infected diabetic wounds

Introduction

The skin is the largest and most exposed organ, with various physiological functions such as protection and supervision, thus playing a crucial role in maintaining bodily homeostasis.[1] Diabetes-related chronic wounds, especially diabetic foot ulcers, can cause persistent pain, eventually leading to amputation and even death, which has always been one of the most common and serious diabetic complications.[2] Compared with ordinary wounds, diabetic wounds are delayed at each healing stage (hemostasis, inflammation, proliferation and remodeling) and tend to develop into chronic or even long-term unhealed

Received: 13 May 2025
Accepted: 29 September 2025
Published: 29 October 2025

wounds.[3] This phenomenon is mainly attributed to the complicated inflammatory microenvironment, including bacterial infection, delayed inflammatory response, reactive oxygen species (ROS) accumulation, and hypoxia conditions.[4–6] In turn, the damaged blood vessels in diabetic wounds hinder blood circulation, leading to insufficient oxygen supply and ultimately exacerbating the inflammatory microenvironment of the wounds.[7] Currently, the common treatment strategy for diabetic wounds is to promote tissue healing by delivering growth factors and eliminate infection through strict debridement.[8,9] However, their single function cannot completely repair the cellular dysfunction caused by persistent hyperglycemia, resulting in unsatisfactory therapeutic effects.[10] In view of the complexity of diabetic wounds, there is a lack of biomaterials that can perform multiple functions in diabetic wound healing, especially bacterial-infected diabetic wounds.

Nanozymes are enzymatically active nanomaterials with advantages such as high stability, low cost, easy large-scale production, low toxicity, and intrinsic enzyme activity, and have attracted widespread attention in their application as substitutes for natural enzymes.[11] The intrinsic enzyme activities of nanozymes mainly include peroxidase (POD)-, oxidase (OXD)-, catalase (CAT)-, and superoxide dismutase (SOD)-like activities.[12] Previous researches have shown that the innate POD and OXD in organisms catalyze a series of substrates, producing ROS to restrict bacterial growth.[13] In addition, inhibiting the elevated concentration of ROS associated with the inflammatory stage can promote wound healing. SOD and CAT are important components of the antioxidant defense system in organisms, which clear ROS by catalyzing the dismutation of superoxide anion radical ($^{\bullet}O_2^-$) to O_2 and H_2O_2 and the conversion of H_2O_2 to H_2O, respectively.[14] Consequently, nanozymes with various enzyme activity should be able to overcome the complex problems in the microenvironment of bacterial-infected diabetic wounds. Therefore, nanozymes have been fabricated for bacterial-infected wound healing by killing pathogenic bacteria,[15,16] regulating the microenvironment,[6] inhibiting inflammation,[17] and modulating macrophage polarization.[18] However, there are certain limitations to current nanozyme-based therapies, such as potential toxicity, limited scalability, and single enzyme activity.

Metal-organic frameworks (MOFs), synthesized via the self-assembly of metal ions and organic ligands, are new functional porous materials, and have attracted substantial interest due to their important features.[19] MOFs have multiple desirable properties that make them suitable for new treatment modalities. For example, ultrathin NiCoCu MOF nanosheets with peroxidase-like activity have been fabricated for accelerating bacteria-infected wound healing.[20] MOFs have been used as drug delivery system due to their structural diversity and high porosity. For example, quercetin-loaded zeolitic imidazolate framework (ZIF-8) continuously releases quercetin and Zn^{2+}, which can promote endothelial cell migration and angiogenesis in diabetic wound healing.[10] MOFs with regular shape and superior ability to accommodate guest nanozymes by anchoring them in appropriate positions have also been combined with nanozymes for bacterial-infected wound healing. For example, Au@ZIF-8 as POD-like catalytic nanozyme has been proposed for bacterial-infected wound healing.[21]

Traditional wound dressings, such as gauze and bandages, are often used to protect wounds from further damage, but these dressings often quickly dry out the wound microenvironment and cause severe pain when replaced.[22] To resolve this problem, hydrogels with three-dimensional hydrophilic polymer networks have received extensive attention as promising materials, because of their excellent porosity, high water content, and soft consistency, which can absorb inflammatory exudates from wounds and maintain a moist environment. Nonetheless, because bacterial-infected diabetic wounds have complex microenvironments, traditional hydrogels with single function usually need to be combined with other functional materials, such as NIR light-driven nanomotor,[23] copper-polyphenol coordination,[24] arginine-doped mesoporous polydopamine nanoparticles,[25] nanoflower composed of glucose oxidase and hemoglobin,[26] glycopeptide,[27] and polypyrrole.[28] The functionalization of hydrogels for accelerating the healing of bacterial-infected diabetic wounds has also been realized by introducing nanozymes, including chitosan-functionalized gold nanoparticles,[29] ultrathin NiCoCu MOF nanosheets,[20] and nanocomposite (Mo,Fe/Cu,I-Ag@GOx).[30] However, the above-mentioned nanozymes have their own drawbacks, such as single enzyme-like activity, cumbersome preparation process, and difficulty in large-scale production. The nanoflower composed of glucose oxidase and hemoglobin has multienzyme-like activity and can effectively promote wound healing of MRSA-infected diabetic wound, but it has the limitations of high price and poor stability.[26] Therefore, it is necessary to develop new multifunctional, inexpensive, stable, and scalable nanozymes for accelerating the healing of bacterial-infected diabetic wounds.

Herein, we established a multifunctional antibacterial chronic wound healing platform. PtPdNi trimetallic nanozyme was formed on the inner wall of MIL-88 pores through an in-situ growth method to obtain PtPdNi trimetallic-doped MIL-88 (PPNM), which exhibited multienzyme-like activity including POD-like, OXD-like, CAT-like, SOD-like, and nicotinamide adenine dinucleotide (NADH) dehydrogenase-like (NAD-like) activities, especially POD-like activity; then PPNM was anchored to polyvinyl alcohol/sodium alginate (PVA/SA) matrix to construct PPNM-containing hydrogel (PPNM-Gel) for accelerating the healing of bacterial-infected diabetic wounds (Figure 1A). PPNM not only exhibited multienzyme-like activity but also had advantages such as high catalytic efficiency, simple preparation, excellent scalability, good stability, and low cost. The PPNM-Gel showed tissue adhesive activity and excellent biocompatibility and could promote the healing of bacterial-infected diabetic wounds mainly by destroying bacteria and alleviating oxidative stress (Figure 1B).

Experimental Method

Chemicals and Materials

$FeCl_3·6H_2O$, 2-aminobenzoic acid (NH_2-BDC), K_2PtCl_4, Na_2PdCl_4, $NiCl_2·6H_2O$, $NaBH_4$, $NaBH_4$, $TiCl_4$, nitro blue tetrazole (NBT), nicotinamide adenine dinucleotide (NADH), $CaCl_2$, methionine, EDTA-Na_2, and *N,N*-dimethylformamide (DMF) were supplied by Aladdin (Shanghai, China). Polyvinyl alcohol (PVA), chitosan (CS), sodium alginate (SA), riboflavin (VB_2), streptozotocin (STZ), and collagenase type II were purchased from Macklin (Shanghai, China). *Staphylococcus aureus* (*S. aureus), Escherichia coli* (*E. coli*), Luria-Bertani (LB) agar plate, and live/dead bacteria staining kit were supplied by Solarbio (Beijing, China). SD male rats (6 weeks, 180–200 g) were purchased from Sibeifu (Beijing, China). Other material and reagent were provided in the Supplementary Material (S 1.1).

Synthesis of PPNM

MIL-88 was first prepared according to the previously reported solvothermal method with minor modifications.[31] In brief, 0.405 g of $FeCl_3·6H_2O$ and 0.249 g of NH_2-BDC were dissolved in 7.5 mL of DMF at round-bottom flask by

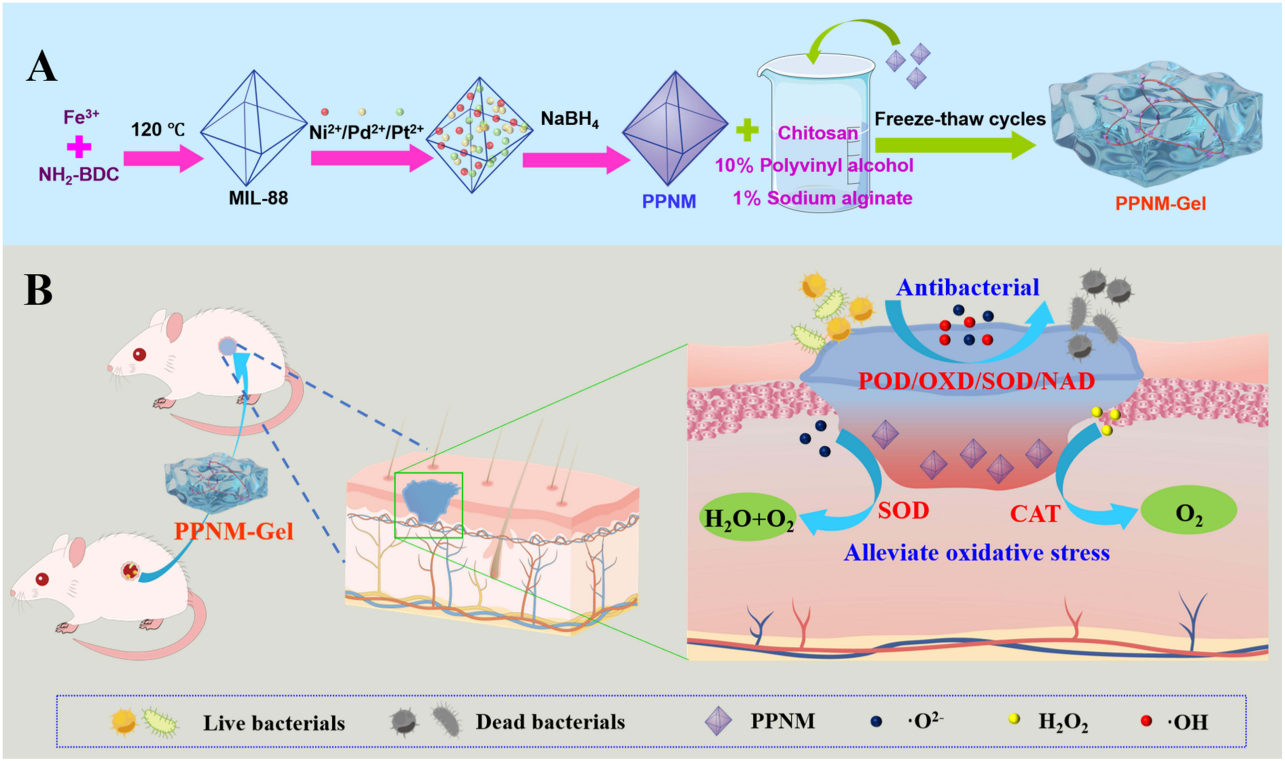

Figure 1 (**A**) Synthetic routes of PPNM and PPNM-Gel. (**B**) Mechanism of PPNM-Gel for accelerating the healing of bacterial-infected diabetic wounds in vivo.

https://doi.org/10.2147/IJN.S540126

vigorous ultrasonication; then, the mixture was vigorously magnetically stirred at 120 °C in an oil bath for 3 h; the fabricated MIL-88 was collected by centrifugation and rinsed with DMF, water and methanol, and obtained after further drying at 60 °C overnight. Then, PtPdNi was doped into MIL-88 by in-situ reduction of Pt^{2+}, Pd^{2+} and Ni^{2+} ions. Briefly, 30 mg of MIL-88 was resuspended in 10 mL of ethanol and further mixed with 0.6 mL of K_2PtCl_4 solution (0.05 mmol mL^{-1}), 0.4 mL of Na_2PdCl_4 solution (0.05 mmol mL^{-1}) and 0.4 mL of $NiCl_2$ solution (0.05 mmol mL^{-1}) for 30 min at ambient temperature; after Pt^{2+}, Pd^{2+} and Ni^{2+} ions fully entered the pores of MIL-88, MIL-88 filled with three ions was collected by centrifugation, washed with water and methanol, and further redistributed in 10 mL of ethanol; subsequently, 1.0 mL of $NaBH_4$ solution (2.0 mg mL^{-1}) was added into the mixture solution, which was gently stirred at ambient temperature for 30 min to achieve in-situ reduction; lastly, the synthetic PPNM was collected, washed, dried and stored at 4 °C.

The molar ratio of Pt^{2+}, Pd^{2+} and Ni^{2+} ions had a serious impact on the enzyme mimicking activity of PPNM. Hence, the orthogonal test was used for investigating the impact degree (ID) of three ions on the POD-like activity of PPNM to optimize the formula. Undoubtedly, the POD-like activity of PPNM increased with the total amount of metal ions loaded onto MIL-88. But when the amount of metal ions was 0.04 mmol, the generated PPNM would aggregate, resulting in poor stability and scalability. Therefore, the selected levels were 0.01 mmol, 0.02 mmol and 0.03 mmol. As showed in Table S1, the three levels of Pt^{2+}, Pd^{2+} and Ni^{2+} ions deemed as three factors in the orthogonal test. The orthogonal array of the nine PPNM was exhibited in Table 1 based on the orthogonal design depicted table L9(33), and the nine PPNM was synthesized by the same procedure except for the different molar ratio of three ions.

Multienzyme-Like Activity of PPNM

The OXD-like activity of PPNM was evaluated by oxidizing TMB. There were three groups, including (*a*) TMB+PPNM, (*b*) TMB+ PPNM (N_2), and (*c*) TMB. Specifically, 20 μL of TMB solution (10 mmol L^{-1}) and 20 μL of PPNM solution (0.05 mg mL^{-1}) were added into 160 μL of acetate buffer (200 mmol L^{-1}, pH=5.0, containing 0.05% Tween-20 and 2% DMSO). The *b* group was pursed with N_2 in advance to remove the dissolved oxygen in the solution. After incubation at

Table 1 Analysis and Results of $L_9(3^3)$ Experimental Design for PtPdNi Trimetallic-Doped MIL-88 (PPNM)

No.	Factor			Absorbance[c]
	A. Pt^{2+} (mmol)	B. Pd^{2+} (mmol)	C. Ni^{2+} (mmol)	
1	0.01	0.01	0.01	0.157
2	0.02	0.01	0.03	0.290
3	0.03	0.01	0.02	0.519
4	0.01	0.02	0.03	0.299
5	0.02	0.02	0.02	0.462
6	0.03	0.02	0.01	0.641
7	0.01	0.03	0.02	0.340
8	0.02	0.03	0.01	0.424
9	0.03	0.03	0.03	0.562
K_1[a]	0.265	0.322	0.407	
K_2[a]	0.392	0.467	0.440	
K_3[a]	0.574	0.442	0.383	
R[b]	0.309	0.145	0.057	
ID of factors	A (Pt^{2+}) > B (Pd^{2+}) > C (Ni^{2+})			
Optimal level	A3-B2-B2: Pt^{2+} (0.03 mmol)-Pd^{2+} (0.02 mmol)-Ni^{2+} (0.02 mmol)			

Notes: [a]The average value of each factor in the level (*i*) was calculated as follows: $K_i=\frac{\sum^{O_i}}{3}$. [b]The range *R* was calculated as follows: R = max{K_i} - min{K_i}. [c]Absorbance: 20 μL of PPNM solution (50 μg mL^{-1}), 20 μL of TMB (10 mM) and 20 μL of H_2O_2 were mixed with 160 μL of acetate buffer (0.2 M, pH 5.0, containing 0.05% Tween-20 and 2% DMSO); after incubation for 5 min, the absorbance of the reaction mixture was detected by Microplate reader at 652 nm.

37 °C for 10 min, the absorption spectra of various groups were recorded by an ultraviolet-visible (UV-Vis) spectrophotometer (Hitachi U-3900, Japan). The POD-like activity of PPNM was also investigated using TMB. The experiments were divided into three groups: (*a*) TMB+H_2O_2+PPNM, (*b*) TMB+H_2O_2, and (*c*) TMB. Each group was pursed with N_2 before adding PPNM. In brief, 20 μL of PPNM solution (0.05 mg mL^{-1}), 20 μL of TMB solution (10 mmol L^{-1}) and 20 μL of H_2O_2 was added into 160 μL of acetate buffer, and the absorption spectra were recorded by an UV-Vis spectrophotometer after incubation at 37 °C for 10 min. The CTA-like activity of PPNM was investigated by decomposing H_2O_2 into O_2, and the H_2O_2 concentration was monitored by $TiCl_4$. The experiments were divided into three groups: (a) $TiCl_4$+H_2O_2+PPNM, (b) $TiCl_4$+H_2O_2, and (c) $TiCl_4$. Briefly, 20 μL of H_2O_2 and 20 μL of PPNM solution (0.05 mg mL^{-1}) were added into 200 μL of pure water, and incubated at 37 °C for 4 h; then 50 μL of above supernatant was mixed with 100 μL of $TiCl_4$ solution (5 mmol mL^{-1}) for 10 min, and the absorption spectra were recorded. The SOD-like activity of PPNM was evaluated based on its $^{\bullet}O_2^-$-scavenging ability by measuring the photoreduction inhibition rate of NBT. There were three groups, including (*a*) VB_2+NBT+PPNM, (*b*) VB_2+NBT, and (*c*) NBT. In short, 50 μL of PPNM solution (0.05 mg mL^{-1}), 100 μL of EDTA-Na_2 solution (0.1 mmol mL^{-1}), 100 μL of methionine solution (0.13 mmol mL^{-1}), 100 μL of VB_2 solution (0.02 mmol mL^{-1}), and 100 μL of NBT solution (0.75 mmol mL^{-1}) were added into 600 μL of Tris-HCl buffer (100 mmol L^{-1}, pH= 8.0). After incubation under illumination for 3 h, the absorption spectra were recorded. The NAD-like activity of PPNM was investigated by monitoring the degradation of NADH in the presence and absence of PPNM. Shortly, 20 μL of PPNM solution (0.05 mg mL^{-1}) and 25 μL of NADH solution (2.0 mmol mL^{-1}) were added into 160 μL of acetate buffer. After incubation under illumination for 30 min, the absorption spectra were recorded.

The steady-state kinetic analyses of PPNM were evaluated by incubating 20 μL of PPNM solution (0.05 mg mL^{-1}) in 160 μL of acetate buffer with different concentrations of TMB and H_2O. After incubation at 37 °C for 10 min, the absorbance values at 652 nm were determined by an UV-Vis spectrophotometer. The Michaelis–Menten equation was used to calculate the kinetic parameters of PPNM as follows:[15]

$$V_o = \frac{V_{max} \times [S]}{K_m + [S]} \tag{1}$$

where, V_o, V_{max}, $[S]$, and K_m indicate initial velocity, maximal reaction velocity (uM^{-1} S^{-1}), substrate concentration (mM), and Michaelis–Menten constant (mM), respectively.

Fabrication of PPNM Loaded Hydrogel

Firstly, 2.0 g of PVA and 80 mg of CS were added into 18.0 mL of water, and the mixture was further stirred at 50 °C to obtain a clear PVA/CS solution. Afterwards, 0.2 g of SA was added into 19.8 mL of water, which was stirred at 50 °C to obtain a 1% SA solution. Subsequently, 5.0 mL of PVA/CS solution and 5.0 mL of 1% SA solution were thoroughly mixed with a certain amount of PPNM; the above sample was frozen at −20 °C and further thawed at ambient temperature for 2 h; after three freeze-thaw treatments, the sample was immersed in 2% $CaCl_2$ solution for 36 h to crosslink the hydrogel. Hydrogels prepared with different PPNM contents (0 mg, 5 mg, 10 mg, 15 mg and 25 mg) were named as PVA/SA-Gel, PPNM5-Gel, PPNM10-Gel, PPNM15-Gel, and PPNM25-Gel, respectively.

Characterization of the Materials

The morphological features of MIL-88, PPNM, PVA/SA-Gel, different PPNM-Gel, and bacteria were exhibited with Sigma 500 scanning electron microscopy (SEM, ZEISS, Germany) or JEM-2100F transmission electron microscopy (TEM, JEOL, Japan). Elemental composition of PPNM was determined by X-MaxN 80T energy dispersive spectroscopy (EDS, Oxford, Britain) equipped on TEM and ESCALAB 250Xi X-ray photoelectron spectroscopy (XPS, Thermo Scientific, USA). Thermogravimetric analysis of MIL-88 and PPNM was performed by a TG 209 F3 thermogravimetric analyzer (Tarsus, Germany). Hydrodynamic particle size and zeta potential of MIL-88 and PPNM were measured using a Nano ZS90 dynamic laser scattering (Malvern, UK). Fourier-transform infrared (FT-IR) spectra of MIL-88, PPNM, PVA/SA-Gel, and different PPNM-Gel were observed by a Nicolet IS 50 FTIR spectrometer (Thermo Scientific, USA) with the KBr disk method.

Swelling Rate and Degradation Rate of PPNM-Gel

Swelling test of PPNM-Gel was completed by evaluating their wet weight change after incubation with phosphate buffer solution (PBS, 20 mmol L^{-1}, pH=7.4). Specifically, the original PPNM-Gel was lyophilized, and its mass was recorded as W_0. Subsequently, the PPNM-Gel was incubated in PBS at 37 °C. After different time intervals (10, 30, 60, 90 and 120 min), the PPNM-Gel was taken out of the PBS and the mass was recorded as W_t. Swelling rate (%) was calculated as $(W_t - W_0)/W_0 \times 100\%$. The measurement was repeated in triplicate with three samples.

The in vitro degradation test was performed by analyzing the mass change of lyophilized PPNM-Gel incubated with collagenase type II over time. The lyophilized PPNM-Gel (M_0) was placed in PBS containing of collagenase type II (0.6 μg mL^{-1}), which was shaken slightly in the incubator at 37 °C. After different time intervals (1, 3, 4, 5, and 7 days), the PPNM-Gel was taken out the incubator, rinsed three times with water, lyophilized, and weighed (M_t). Degradation rate (%) was calculated as $M_t / M_0 \times 100\%$. The measurement was also repeated in triplicate with three samples.

In vitro Evaluation of PPNM-Gel

The cytocompatibility of different PPNM-Gel was evaluated with L929 cells and human umbilical vein endothelial cells (HUVEC-SV40). Further details were provided in the Supplementary Materials S 1.2 and 1.3. The in vitro antimicrobial effects of different PPNM-Gel were evaluated using *S. aureus* and *E. coli*, which were sub-cultured in appropriate media. For evaluating the effects of PPNM-Gel on the growth of bacteria, 0.1 mL of *S. aureus* or *E. coli* suspension (2×10^8 CFU mL^{-1}) were mixed with PVA/SA-Gel or different PPNM-Gel (50 mg). After incubation for 4 h at 37 °C, 50 μL of bacterial solution was aspirated and pipetted onto LB agar plates. After incubation for 24 h at 37 °C, the bacterial growth of each group was examined, and the total number of bacterial colonies were counted. For bacteriostatic ring test, 50 μL of *S. aureus* or *E. coli* suspension (1×10^8 CFU mL^{-1}) were uniformly coated on LB agar plates, respectively; the PVA/SA-Gel or PPNM-Gel soaked in 0.03% H_2O_2 solution was placed on the LB agar plates, and then the LB agar plates were placed at 37 °C; after 18 h, the results of the bacteriostatic ring were assessed and recorded. To further investigate the antibacterial properties of PPNM-Gel, the bacterial suspension (2×10^8 CFU/mL) was mixed with PVA/SA-Gel or different PPNM-Gel (50 mg) soaked in 0.03% H_2O_2 solution. After incubation for 4 h, the bacteria were washed three times with PBS, and then stained with NucGreen or EthD-III for about 30 min according to the manufacturer's instructions. Subsequently, the prepared bacteria were observed under an inverted fluorescence microscope (Leica DMI3000B, Germany). In vitro biofilm assay was provided in the Supplementary Material (S 1.4).

In vivo Antibacterial and Wound Healing Evaluation

SD male rats were used to establish a diabetic animal model by using STZ (80 mg kg^{-1}). STZ solution (10 mg mL^{-1}) was prepared in the sodium citrate buffer solution (0.1 mol L^{-1}, pH 4.0). After at least four consecutive days of intraperitoneal injection, the blood glucose levels of rats were tested, and the rats with blood glucose levels greater than 300 mg dL^{-1} were defined as diabetic rat for the subsequent experiments. STZ-induced diabetic SD rats were anesthetized with 5% chloral hydrate and their backs were shaved and disinfected. Subsequently, a circular wound with 7 mm diameter was made by cutting off the full-thickness skin, and then 0.1 mL of *S. aureus* and *E. coli* suspension (2×10^8 CFU mL^{-1}) was seeded on the wound. These rats with bacterial-infected diabetic wounds were randomly divided into six groups with different treatments: PBS (Control group), PVA/SA-Gel, PPNM5-Gel, PPNM10-Gel, PPNM15-Gel and PPNM25-Gel. All hydrogels (cylinder with a diameter of 1.4 cm and a height of 0.6 cm) were secured with gauze and bandage and replaced every 24 h. During the treatment period, the rats were observed daily, and the wound area of each group was measured on the 0th, 3th, 6th, 9th and 12th day, respectively. On the 12th day, the rats were euthanized and the wound tissues of each group were collected. The wound tissue was fixed with 4% formaldehyde, and then paraffin sections with thickness of 3–5 mm were made for hematoxylin and eosin (H&E) staining, Masson staining and immunofluorescence staining. Further details are provided in the Supplementary Material (S 1.5).

Results and Discussion

Fabrication and Characterization of PPNM

MIL-88 possesses large surface area and high porosity. Therefore, Pd^{2+}, Pt^{2+} and Ni^{2+} ions could enter the pores of MIL-88 and then $NaBH_4$ solution reduced these ions in situ to form trimetallic nanozyme on the inner wall of MIL-88 pores. Pd, Pt, and Ni were chosen because they belong to different cycles of Group VIII elements, and are inexpensive and highly safe. To optimize the molar ratio of Pt^{2+}, Pd^{2+}, and Ni^{2+} ions, the POD-like activity of PPNM served as the evolution index of the orthogonal test. As listed in Table 1, the formula composition of three ions influenced the POD-like activity. For example, when the factor A (Pt^{2+}) was at level 3 (0.03 mmol), the K_3 was expressed mathematically as: (0.519 + 0.641 + 0.562)/3 = 0.574, which indicated the cumulative value of factor A at the level 3. The maximum K_i values of three ions were underlined. Pt^{2+} ion possessed the highest R value, and the most important impact for the POD-like activity of PPNM, followed by Pd^{2+} and Ni^{2+} ions. Within the set range, the trends of K_i indicated that the POD-like activity enhanced with increasing dosage of Pt^{2+} ion and increased first and then decreased with increasing dosage of Pd^{2+} and Ni^{2+} ions. According to the orthogonal test, the optimal formula composition was 0.03 mmol of Pt^{2+} ion, 0.02 mmol of Pd^{2+} ion, and 0.02 mmol of Ni^{2+} ion.

The structure and morphology of MIL-88 and PPNM were investigated through SEM and TEM. The prepared MIL-88 nanoparticles showed smooth surface and uniform polygonal-like nanostructure (Figure 2A). Dynamic laser scattering revealed that the average hydrodynamic size of MIL-88 was about 180 nm (Figure S1). Based on the SEM and TEM images, the synthesized PPNM still exhibited uniform polygonal-like nanostructure (Figure 2B), but its surface had become rough (Figure 2C). This indicated that PtPdNi trimetallic nanoparticles were decorated onto the interior and surface of MIL-88. The average hydrodynamic size of PPNM was about 195 nm (Figure S1), and approximately 15 nm larger than that of the MIL-88 due to the modification of PtPdNi trimetallic nanoparticles. The PPNM was further observed by the EDS elemental mapping. The elemental mapping exhibited that the PPNM contained C, N, O, Fe, Pt, Pd, and Ni elements and the Pt, Pd, and Ni elements were uniformly distributed throughout the nanostructure (Figure 2D).

MIL-88 exhibited a positive zeta potential (26.8 mV) because of the presence of exposed amino groups (Figure S2). After the amino groups were covered by PtPdNi trimetallic nanoparticles, the zeta potential of PPNM rapidly dropped to 16.2 mV. XPS was also used to evaluate the chemical composition of PPNM (Figure 2E). The binding energies at 71.5, 284.8, 335.7, 400.0, 532.0, 711.7, and 856.1 eV were attributed to the characteristic peaks of Pt4f, C1s, Pd3d, N1s, O1s, Fe2p, and Ni2p, respectively. The compositions of MIL-88 and PPNM were also investigated by thermogravimetric analysis (Figure 2F). Certainly, the weight gradually decreased with the increase of temperature. Below 200 °C, the weight loss mainly resulted from the volatilization of unstable components; above 200 °C, the weight loss originated from the destruction of MIL-88 and further degradation of organic components. The maximum weight losses of PPNM and MIL-88 at 800 °C were 55.0% and 61.3%, respectively. The result suggested that the PtPdNi trimetallic nanozyme accounted for about 10.3% of the total mass of PPNM, which confirmed the successful modification of PtPdNi trimetallic nanoparticles on the MIL-88.

Multienzyme-Like Activity of PPNM

TMB was selected as the reaction substrate to evaluate the catalytic performance of PPNM, because it can be oxidized to a blue oxidized TMB (TMB_{ox}) with an obvious absorption peak at 652 nm. The TMB group had no absorption peak, but the TMB+PPNM group exhibited a remarkable absorption peak at 652 nm (Figure 3A). Meanwhile, the absorption peak of TMB+PPNM (N_2) group obviously reduced after N_2 blowing. This demonstrated that the quantity of TMB_{ox} was closely related to the dissolved oxygen in the solution, which played a crucial role in the oxidation process of TMB involving PPNM. Therefore, PPNM had OXD-like catalytic activity, which catalyzed the production of ROS from oxygen to oxidize TMB for color development. The POD-like activity of PPNM also chose TMB as the substrate for the colorimetric reaction. To reduce the impact of OXD-like catalytic activity, the reaction buffer was purged with N_2 to remove dissolved oxygen. As depicted in Figure 3B, both TMB and TMB+H_2O_2 groups did not show significant absorption peaks. Conversely, the TMB+H_2O_2+PPNM group exhibited a robust absorption peak. This result demonstrated that PPNM possessed POD-like catalytic activity, which catalyzed the production of ROS from H_2O_2 and thereby oxidized TMB for colorimetric reaction. The CAT-like activity of PPNM was evaluated by measuring its ability to

 https://doi.org/10.2147/IJN.S540126

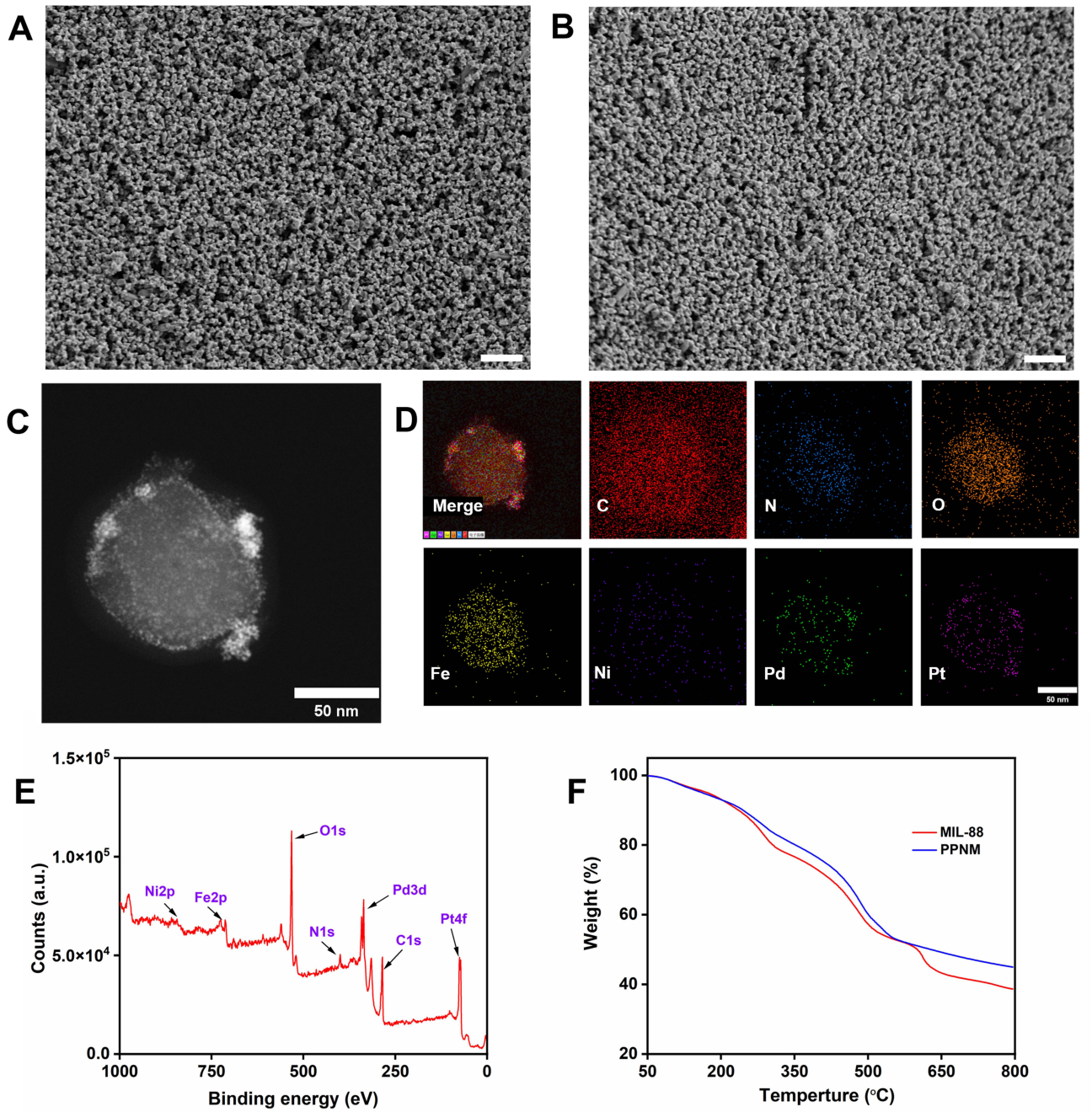

Figure 2 (**A** and **B**) Representative SEM images of MIL-88 (**A**) and PPNM (**B**); bar = 1 μm. (**C** and **D**) Representative TEM image (**C**) and EDS elemental mapping (**D**) of PPNM; bars = 50 nm. (**E**). XPS of PPNM. (**F**) Thermogravimetric analysis of MIL-88 and PPNM.

decompose H_2O_2 into O_2 through the H_2O_2 concentration measurement. $TiCl_4$ was used to monitor the H_2O_2 concentration, because it can react with H_2O_2 to form a yellow complex $[TiO(H_2O_2)]^{2+}$ with a characteristic absorption at 412 nm (Figure 3C, H_2O_2+$TiCl_4$ group). After treatment with PPNM, the absorption peak significantly decreased (Figure 3C, H_2O_2+$TiCl_4$+PPNM group), indicating that PPNM possessed obviously CAT-like activity. In the presence of oxidizing substances, VB_2 is reduced under light conditions to generate $^{\bullet}O_2^-$, which can reduce NBT to blue methylhydrazine with a characteristic absorption at about 560 nm. The photoreduction inhibition rate of NBT was used to evaluate the SOD-like activity of PPNM (Figure 3D). As expected, the VB_2+NBT group showed a remarkable absorption peak. Instead, the absorption peak dramatically decreased after treatment with PPNM. This demonstrated the excellent SOD-like activity of

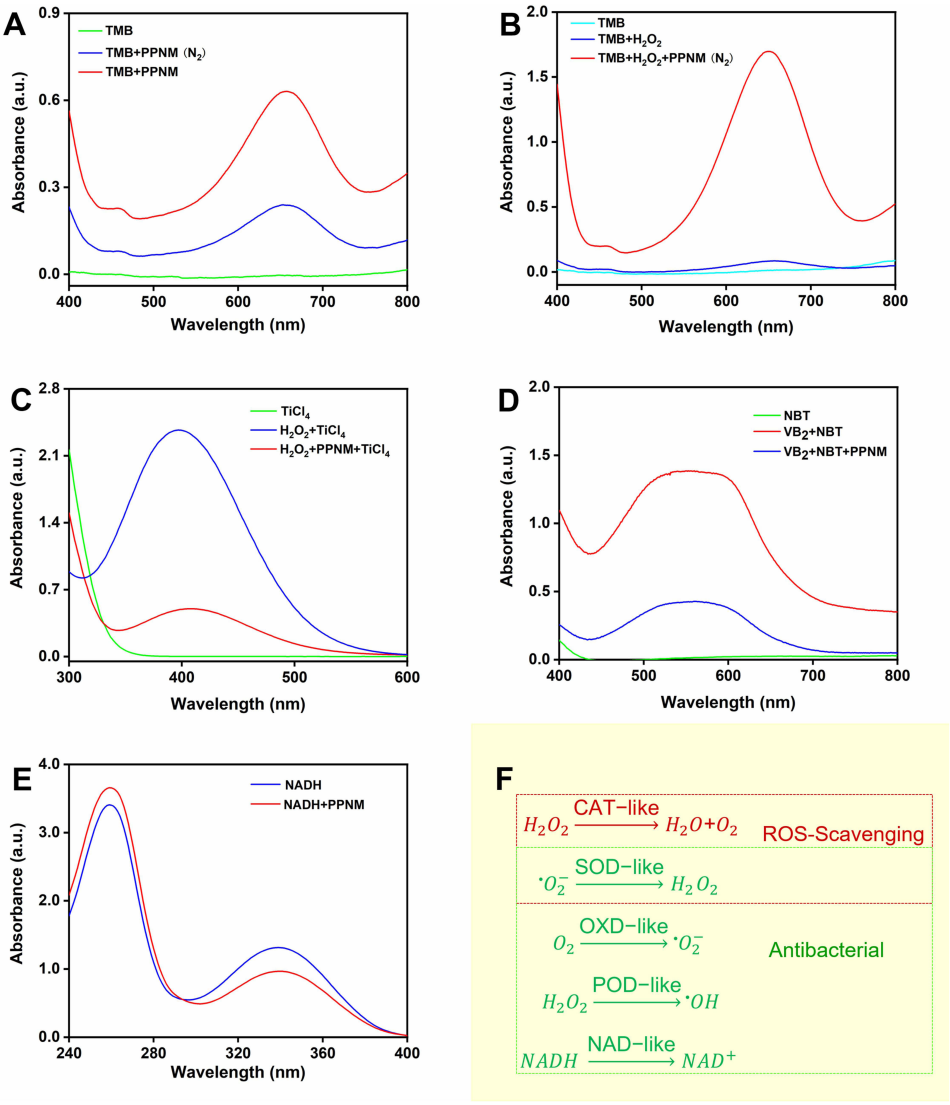

Figure 3 (**A**–**E**) UV-vis spectra for OXD-like (**A**), POD-like (**B**), CAT-like (**C**), SOD-like (**D**) and NAD-like (**E**) activities. (**F**) Multienzyme-like activity and corresponding ability of PPNM.

PPNM. In the presence of NADH dehydrogenase, NADH undergoes oxidative dehydrogenation to form to NAD^+, which is involved in the regulation of energy production and cellular metabolism.[32] The NAD-like activity of PPNM was investigated by monitoring the degradation of NADH and the generation of NAD^+ in the presence of PPNM. NADH exhibits unique absorption at wavelengths of 260 and 340 nm, while NAD^+ only shows significant absorption at 260 nm. Certainly, the UV spectrum of NADH exhibited significant absorption at 260 and 340 nm (Figure 3E). After the addition of PPNM, the absorption peaks at 340 nm and 260 nm obviously decreased and increased, respectively. The result suggested that PPNM could catalyze the conversion of NADH to NAD^+ through NAD-like activity.[15]

Bacterial-infected wounds possess complex microenvironments, including bacterial infection and ROS accumulation. Nanozyme can catalyze the production of ROS to kill bacteria and promote the healing of bacterial-infected wounds. The mechanism of generating ROS could be divided into the following steps: nanozyme catalyzes the conversion of O_2 to $^{\bullet}O_2^-$ through OXD-like activity; then $^{\bullet}O_2^-$ is decomposed into H_2O_2 through SOD-like activity; ultimately, •OH is generated under the influence of POD-like activity.[33] ROS (•OH) can also catalyze the generation of exogenous H_2O_2 through POD-like activity of nanozyme.[20] Nanozyme can also promote the healing of bacterial-infected wounds by ROS-scavenging. Briefly, nanozyme catalyzes the conversion of $^{\bullet}O_2^-$ to H_2O_2 through SOD-like activity, and then H_2O_2 is decomposed into H_2O and O_2

https://doi.org/10.2147/IJN.S540126

through CTA-like activity. Specifically, PPNM exhibited significant multienzyme-like activity, including OXD-like, POD-like, CTA-like, SOD-like, and NAD-like activity (Figure 3F). In other words, the OXD-like, POD-like, SOD-like, and NAD-like activities of PPNM can achieve antibacterial effects through blocking ATP synthesis and ROS-mediated bacterial oxidative damage, while the CTA-like and SOD-like activities of PPNM can complete ROS-scavenging. PPNM exhibited more enzyme-like activity than previously reported trimetallic nanozyme with single enzyme activity, for example, ultrathin NiCoCu MOF nanosheets only showed POD-like activity;[20] PPNM also had a regular structure, making it easier to replicate and scale compared to other materials with multienzyme-like activity, including nanoflower composed of glucose oxidase and hemoglobin,[26] nanocomposite (Mo,Fe/Cu,I-Ag@GOx)[30] and AuCu@CuO_2 aerogel.[34] This indicated that the PPNM had advantages such as simple preparation, excellent scalability, good stability, and low cost.

To deeply evaluate catalytic efficiency of PPNM, the K_m and V_{max} were measured. The OXD-like steady-state kinetics of PPNM were evaluated by altering the TMB concentration. The reaction velocity was significantly correlated with TMB concentration (Figure 4A). According to Michaelis-Menten equation (Figure 4B), the K_m and V_{max} values were 0.066 mM

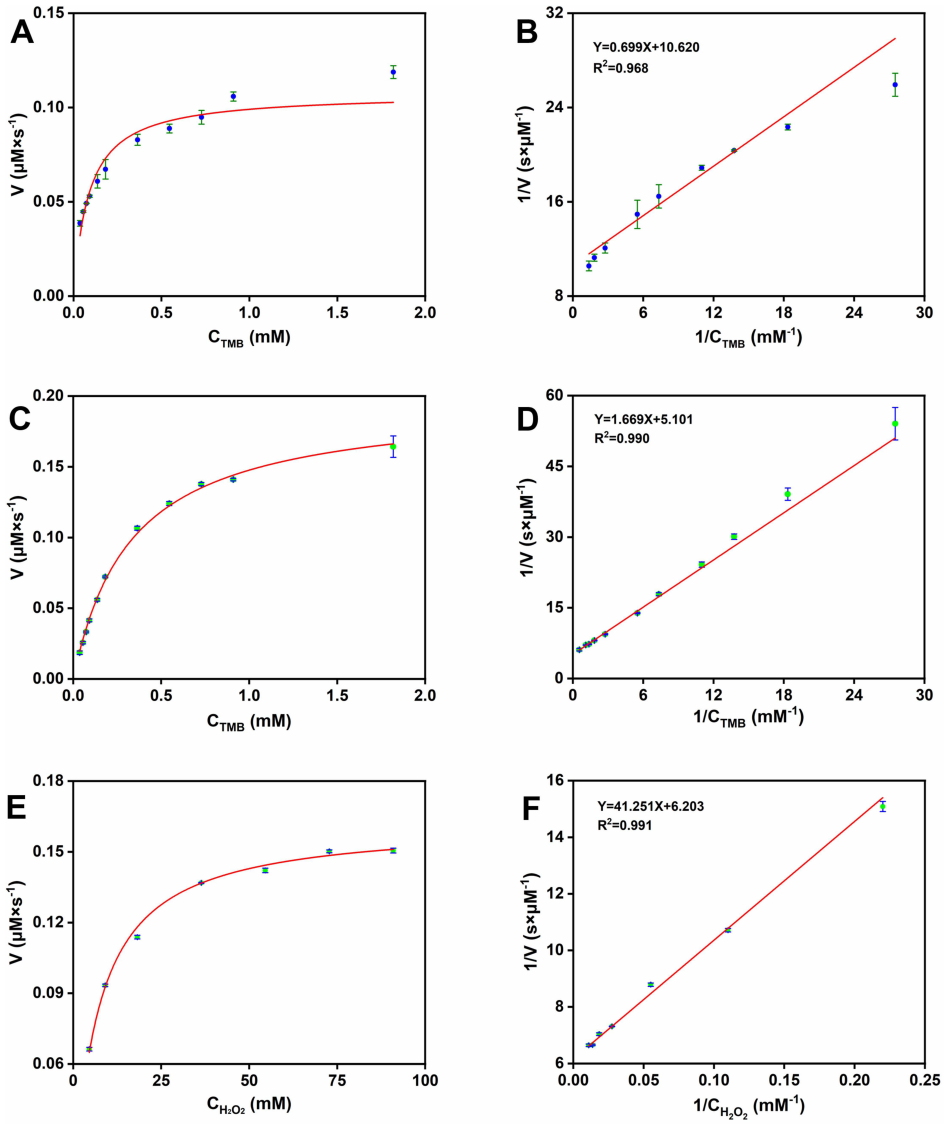

Figure 4 (**A**) Steady-state kinetics of oxidase-like activity of PPNM with TMB as a substrate. (**B**) Double-reciprocal plot of oxidase-like activity of PPNM with TMB as a substrate. (**C**) Steady-state kinetics of peroxidase-like activity of PPNM with TMB as a substrate. (**D**) Double-reciprocal plot of peroxidase-like activity of PPNM with TMB as a substrate. (**E**) Steady-state kinetics of peroxidase-like activity of PPNM with H_2O_2 as a substrate. (**F**) Double-reciprocal plot of peroxidase-like activity of PPNM with H_2O_2 as a substrate.

and 0.094 μM^{-1} S^{-1}, respectively. Compared with other reported OXD-like nanozymes,[15,35–38] the lower K_m of PPNM indicated the stronger enzyme affinity toward the substrate and the excellent OXD-like activity (Table S2). By varying the TMB and H_2O_2 concentrations, the POD-like steady-state kinetics of PPNM were investigated (Figure 4C–F). The TMB (Figure 4C) and H_2O_2 (Figure 4E) concentrations significantly affected the reaction velocity. The kinetic parameters of PPNM in POD-like activity were also calculated from the Michaelis–Menten equation. The K_m and V_{max} values of TMB substrate on PPNM (Figure 4D) were 0.327 mM and 0.196 μM S^{-1}, respectively, while the K_m and V_{max} values of H_2O_2 substrate Figure 4F) were 6.650 mM and 0.161 μM S^{-1}, respectively. Compared with the previously reported nanozymes,[15,20,39–43] PPNM often exhibited a lower K_m and a higher V_{max} (Table S3). Specifically, PPNM and ultrathin NiCoCu MOF nanosheets[20] were both trimetallic nanozymes with the same level of catalytic ability, but PPNM had a wider variety of enzyme-like activity. The results indicated that PPNM had superior affinity toward the substrate and great potential for application in sterilization due to the excellent multienzyme-like activity.

Fabrication and Characterization of PPNM-Gel

SEM image analysis of PVA/SA-Gel and PPNM-Gel was conducted and showed their cross-sectional structural morphology (Figure 5A–E). These hydrogels exhibited three-dimensional network porous structure, which provided channels for water molecules to enter and leave quickly and were also the basis for PVA/SA-Gel to load PPNM. The

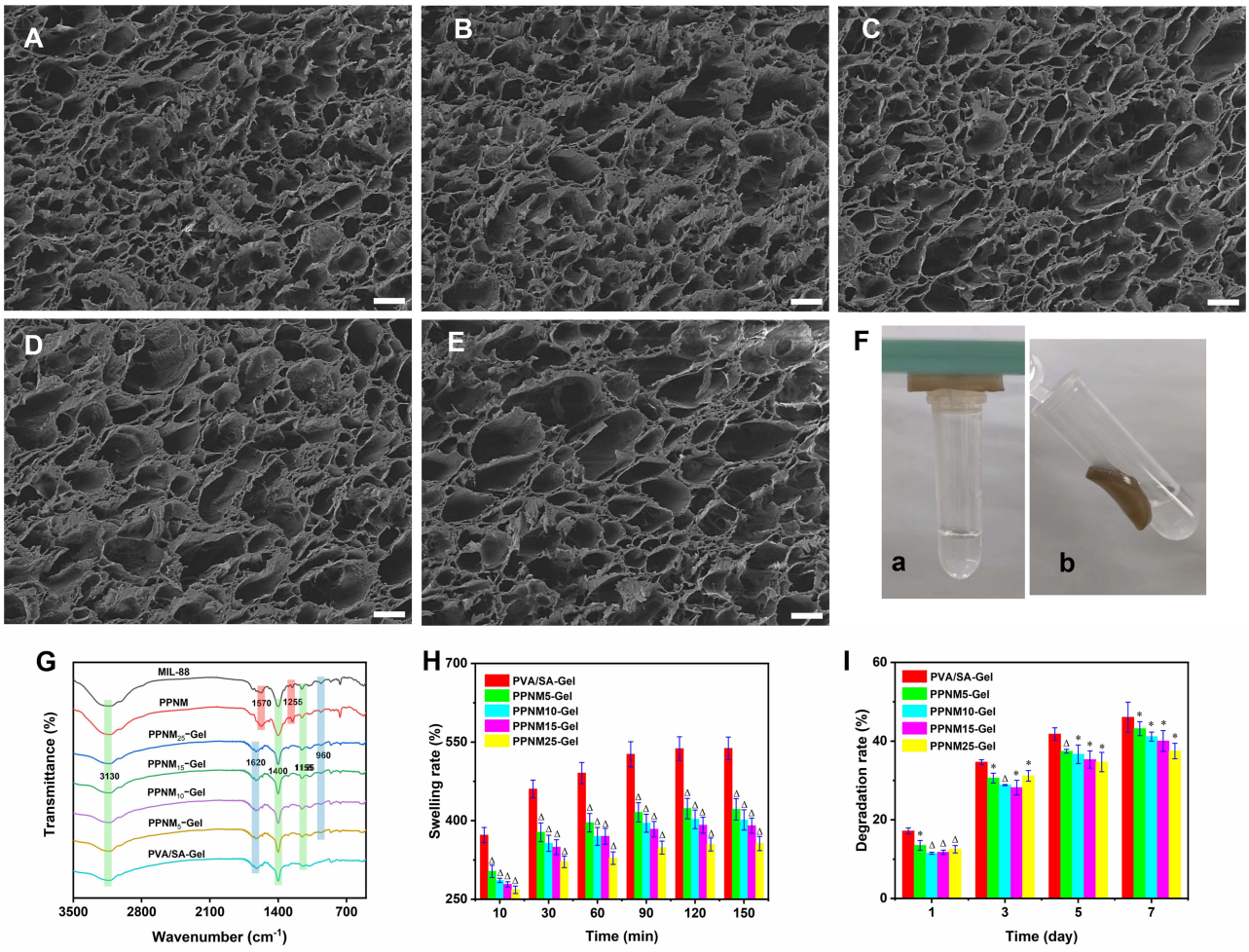

Figure 5 (**A**–**E**) Representative SEM images of PVA/SA-Gel (**A**) PPNM5-Gel (**B**) PPNM10-Gel (**C**) PPNM15-Gel (**D**) and PPNM25-Gel (**E**); bars = 20 μm. (**F**) Photographs about the adhesive property of PPNM-Gel. (**G**) FT-IR spectra of PVA/SA-Gel and different PPNM-Gel. (**H**) Swelling ratio of PVA/SA-Gel and different PPNM-Gel ($^{\Delta}$Denotes $P < 0.05$ compared with the PVA/SA-Gel). (**I**) degradation behavior of PVA/SA-Gel and different PPNM-Gel (*Denotes $P > 0.05$ compared with the PVA/SA-Gel; $^{\Delta}$Denotes $P < 0.05$ compared with the PVA/SA-Gel).

https://doi.org/10.2147/IJN.S540126

macroporous structure could reduce the resistance of PPNM transfer and was beneficial for PPNM release to the wound site. The pore sizes of PVA/SA-Gel, PPNM5-Gel, PPNM10-Gel, PPNM15-Gel, and PPNM25-Gel (Figure S3) were 9.03 ±1.41 μm, 10.56±0.45 μm, 14.35±1.08 μm, 15.85±1.53 μm, and 17.72±1.26 μm, respectively. This result indicated that the introduction of PPNM slightly increased the pore size of PPNM-Gel. In addition, the PPNM-Gel could be firmly attached to the glass plate without peeling even with gravity stretching (Figure 5F). PPNM-Gel contained a large number of hydrogen bond donors and receptors, leading to the formation of physical adsorption through hydrogen bond between the silica bond on the glass surface and the hydrophilic polymer of PPNM-Gel. The skin surface also contains a large number of hydrogen bond donors and acceptors. This suggested the presence of the excellent adhesion between PPNM-Gel and skin, which could prevent the PPNM-Gel from falling off, thereby helping to avoid wound exposure. This would avoid frequent replacement of PPNM-Gel dressings and reduce further damage to the wounds.

The successful fabrication of PPNM-Gel was further proved by the FT-IR spectra (Figure 5G). For PPNM, the characteristic peaks at 1570 cm^{-1}, 1255 cm^{-1}, and 960 cm^{-1} were the vibration of benzene ring skeleton ($\nu_{C=C}$), in-plane bending vibration of aromatic hydrogen ($\beta_{=C-H}$), and out-of-plane bending vibration of aromatic hydrogen ($\gamma_{=C-H}$), indicating the presence of benzene ring; the characteristic peaks at 3130 cm^{-1}, 1155 cm^{-1}, and 1400 cm^{-1} were the stretching vibration of N-H bond (ν_{N-H}) of amino group, stretching vibration of C-N bond (ν_{C-N}), and stretching vibration of C=O bond ($\nu_{C=O}$) of carboxyl group, which originated from 2-aminobenzoic acid. For PVA/SA-Gel, the mingle peak at 3130 cm^{-1} might be attributed to the stretching vibration of N-H bond (ν_{N-H}) and O-H bond (ν_{O-H}); the peaks at 1620 cm^{-1}, 1400 cm^{-1}, and 1155 cm^{-1} might be devoted to the stretching vibration of C=O bond ($\nu_{C=O}$), bending vibration of C-H (δ_{C-H}), and the stretching vibration of C-O bond (ν_{C-O}), which resulted from PVA, CS and SA. After loading PPNM into PVA/SA-Gel, most of the characteristic peaks shifted or overlapped with other peaks, but the characteristic peak of out-of-plane bending vibration of aromatic hydrogen ($\gamma_{=C-H}$) was still observed at 960 cm^{-1}, indicating the successful fabrication of PPNM-Gel.

Swelling features of PPNM-Gel were investigated under physiological environment in PBS at 37 °C. The swelling rates of different hydrogels increased first and then tended to equilibrium with time and reached the maximum at 120 min (Figure 5H). Furthermore, the swelling rates exhibited a decreasing trend with increasing PPNM content. It was mainly because the PPNM occupied the internal space of hydrogel and competed with water molecules for the hydration position in the hydrogel, thus reducing the swelling rate of hydrogel. However, the highest swelling rate of different PPNM-Gel was higher than 350%. The result demonstrated that the PPNM-Gel possessed excellent water absorption ability. Accordingly, the PPNM-Gel could effectively absorb considerable inflammatory exudates from bacterial-infected wounds and prevent them from accumulating around the wounds.[16] This process could promote the healing of bacterial-infected diabetic wounds, positioning PPNM-Gel as a potential ideal dressing for the treatment of bacterial-infected diabetic wounds. Degradability of PPNM-Gel was further investigated by measuring the mass change of dry hydrogels under physiological conditions. The degradation rate of all hydrogels undoubtedly increased with time, and usually decreased with increasing PPNM concentration, especially on the 7th day (Figure 5I). The PPNM provided many interaction sites for the hydrogel, which enabled the PPNM-Gel to have a more compact three-dimensional network structure, thereby mitigating degradation. The PPNM-Gel exhibited excellent degradation performance and could effectively release PPNM during treatment. Moreover, the PPNM-Gel could be easily removed, thereby further improving the healing effect of bacterial-infected diabetic wounds.

Biocompatibility of PPNM-Gel

The biocompatibility of biomaterials is crucial for clinical applications. The cytocompatibility of different PPNM-Gel was evaluated by co-culturing their extracts with L929 cells. The viability of L929 cells in various groups was assessed through MTT assay. Figure 6A illustrated the treatment of L929 cells with different hydrogel extracts for 24 h. Compared to the PVA/SA-Gel, the viability of L929 cells exposed to different PPNM-Gel extracts was all higher than 91.4%, suggesting that cell activity was still strong. With increasing the PPNM concentration, PPNM-Gel extracts showed negligible cytotoxicity, indicating that it was mostly nontoxic to cells within the studied concentration range and safe to use. Scratch test was used to evaluate the effect of PPNM-Gel extracts on the HUVEC-SV40 migration. The migration distance of HUVEC-SV40 increased significantly with prolonged incubation time (Figure S4), while it exhibited

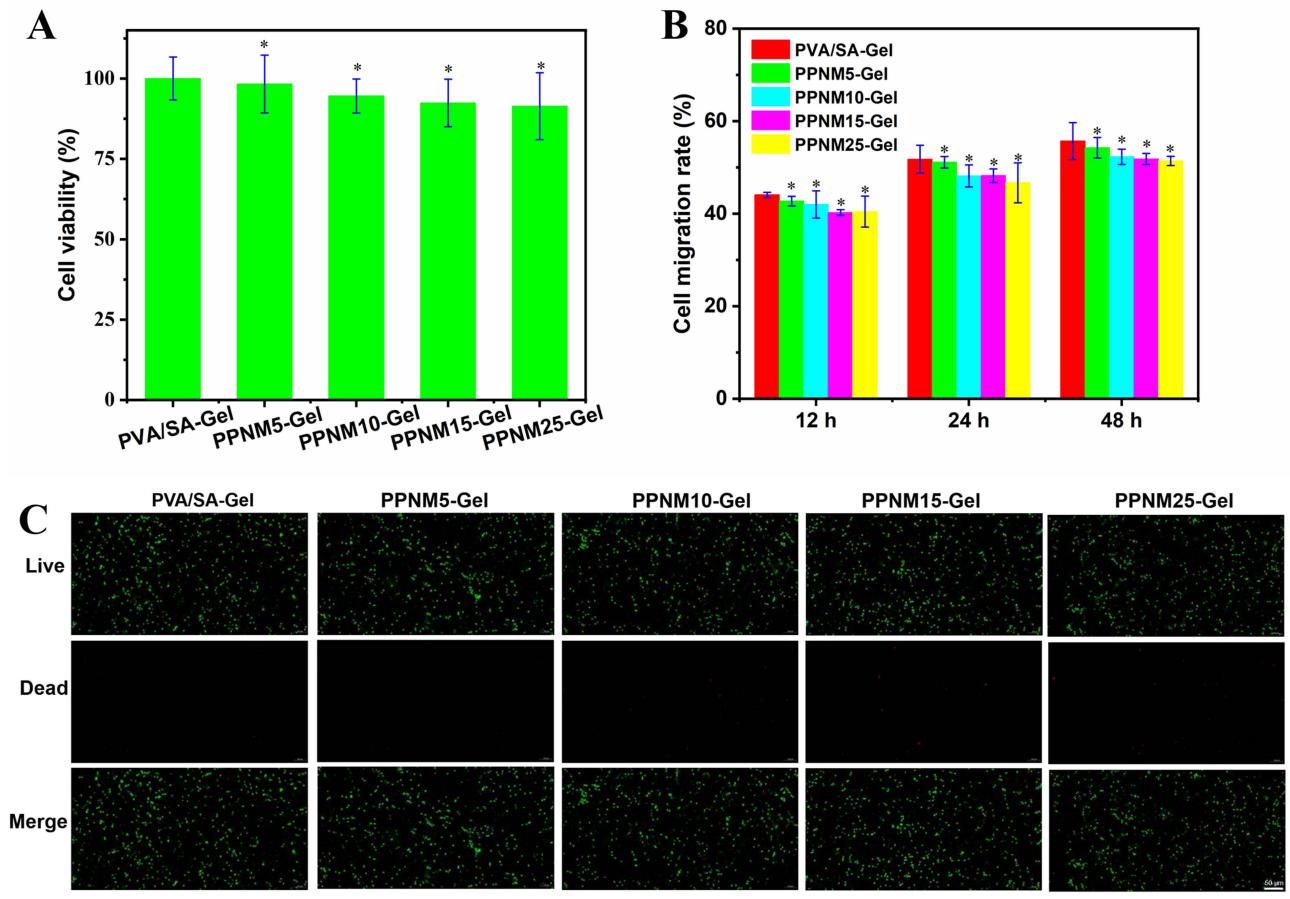

Figure 6 (**A**) L929 cell viability after incubation with different hydrogel extracts for 24 h (*Denotes $P > 0.05$ compared with the control group). (**B**) Cell migration rate of HUVEC-SV40 after incubation with different hydrogel extracts for 12, 24 and 48 h (*Denotes $P > 0.05$ compared with the control group at same time). (**C**) Live/dead L929 cell staining results after incubation with different hydrogel extracts for 24 h, bar = 100 μm.

a negligible decrease with the increase of PPNM concentration, as the difference was not statistically significant (Figure 6B). Subsequently, the impact of PPNM-Gel extracts on the viability of L929 cells was further conducted via live/dead cell staining. The vast majority of L929 cells in the experimental groups showed vitality (green fluorescence), with only a very small number of dead cells (red fluorescence) observed in PPNM15-Gel and PPNM25-Gel (Figure 6C). This was consistent with the finding from MTT assay and further suggested good biocompatibility of PPNM-Gel.

In vitro Antibacterial Ability of PPNM-Gel

The abundant exudate and high glucose environment around the diabetic wounds not only lead to excessive inflammation response but also provide a suitable medium for persistent bacterial infection.[44] Generous nanozymes been reported to exhibit antibacterial effects by catalyzing the production of large amounts of ROS.[45] The above study highlighted that PPNM exhibited excellent POD-like and OXD-like activities and could promote the production of harmful ROS from H_2O_2 and O_2 in the environment. Bacteria produce endogenous H_2O_2 through metabolism,[46] which can serve as a substrate for PPNM catalysis, generating ROS and effectively enhancing the antibacterial activity of PPNM. In addition, the NAD-like activity of PPNM may lead to depletion of NADH in bacteria, thereby disrupting their redox balance and inhibiting metabolism, resulting in antibacterial effects. Accordingly, the study investigated the in vitro antibacterial activity of PPNM-Gel against Gram-positive *S. aureus* and Gram-negative *E. coli*. Compared with the control group, all treatment groups showed a notable reduction in the number of bacterial colonies on the agar plate (Figure 7A); the number of colonies in the PPNM-Gel was significantly lower than that in the PVA/SA-Gel (Figure 7B); the antibacterial ability of PPNM-Gel against *E. coli* was stronger than that against *S. aureus*, especially for PPNM10-Gel

https://doi.org/10.2147/IJN.S540126

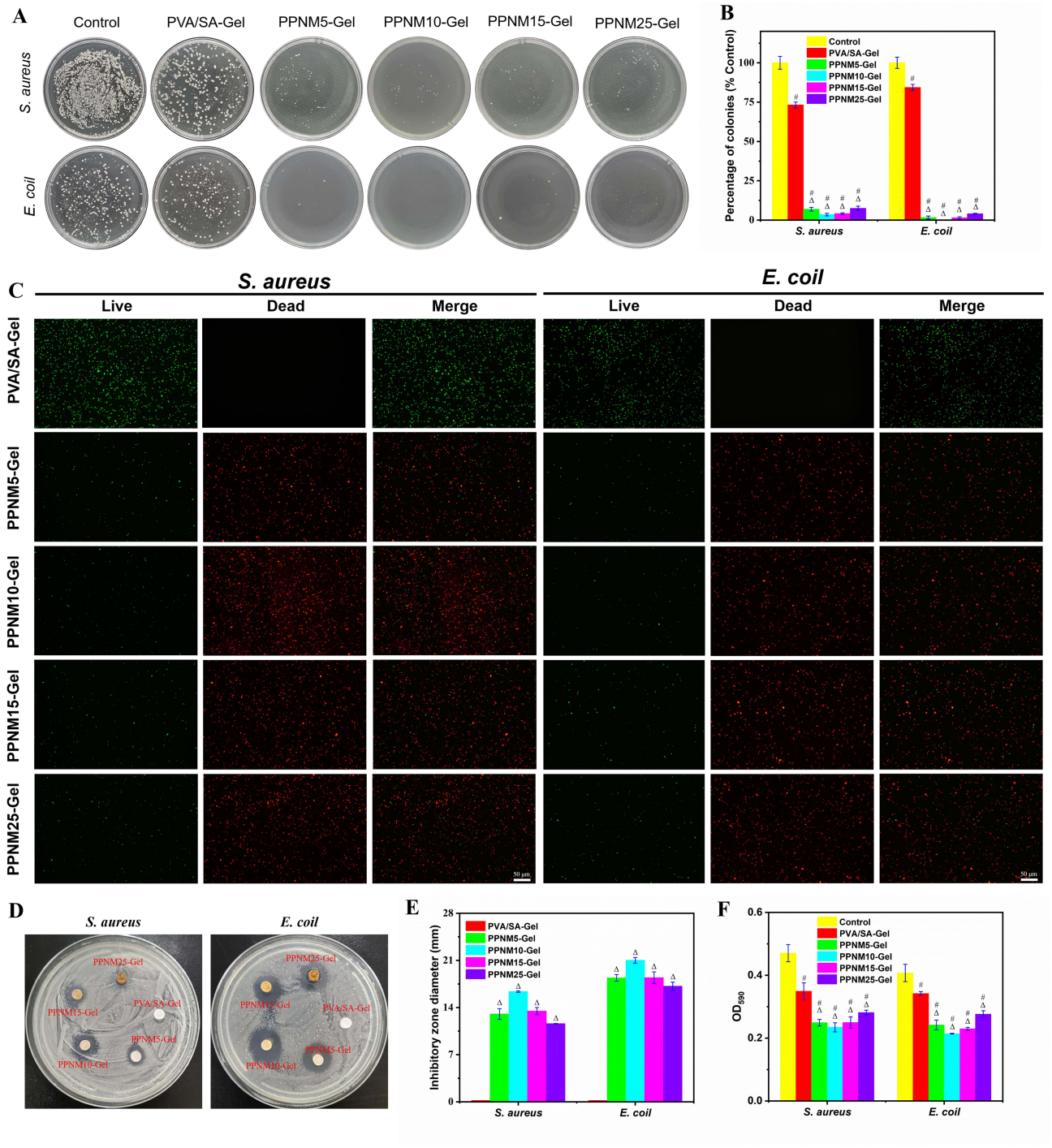

Figure 7 (**A**) Pictures of colonies growth of *S. aureus* and *E. coli* on agar plates after treatment with control, PVA/SA-Gel and different PPNM-Gel. (**B**) The percentage of *S. aureus* and *E. coli* colonies (n =3) after different treatments ($^{\#}$Denotes $P < 0.05$ compared with the control group; $^{\Delta}$Denotes $P < 0.05$ compared with the PVA/SA-Gel). (**C**) Live/dead bacterial cells staining images of *S. aureus* and *E. coli* after different treatments, bars = 50 μm. (**D**) Pictures of *S. aureus* and *E. coli* suppression rings after treatment with PVA/SA-Gel and different PPNM-Gel. (**E**) Quantitative analysis of *S. aureus* and *E. coli* suppression ring diameter after different treatments ($^{\Delta}$Denotes $P < 0.05$ compared with the PVA/SA-Gel). (**F**) Absorbance values of *S. aureus* and *E. coli* biofilm after different treatments ($^{\#}$Denotes $P < 0.05$ compared with the control group; $^{\Delta}$Denotes $P < 0.05$ compared with the PVA/SA-Gel).

(Figure 7B). According to SEM images (Figure S5), *S. aureus* and *E. coli* in the control group had flat surfaces and intact cell structures. After exposure to PVA/SA-Gel, there was no significant change in the morphology and membrane integrity of the two bacteria. After treatment with PPNM-Gel, both bacteria suffered severe damage, including significant loss of membrane integrity and potential cell lysis.[15] Furthermore, *E. coli* and *S. aureus* treated with different methods

were stained with NucGreen/EthD-III dyes and photographed under an inverted fluorescence microscope, where red and green fluorescence represented dead and live bacteria, respectively. As shown in Figure 7C, all PPNM-Gel groups exhibited obvious red fluorescence, demonstrating massive bacterial mortality. Instead, the PVA/SA-Gel only showed green fluorescence, indicating bacterial survival. These results confirmed previous antibacterial tests and emphasized the significant antibacterial efficacy of PPNM-Gel. The results of bacteriostatic ring test further confirmed the bactericidal ability of PPNM-Gel against the pathogenic bacteria (Figure 7D and E). The antibacterial effect of PPNM-Gel against *E. coli* was higher than that against *S. aureus*, and the PPNM10-Gel exhibited the strongest antibacterial effect.

Most bacterial infections are accompanied by the production of bacterial biofilms. Bacterial biofilms exhibit high tolerance to host immune defense mechanisms and antibiotics, as they are composed of dense bacterial aggregates and protected by dense extracellular polymeric substances.[32] Therefore, killing free pathogens is usually the first step in antibacterial treatment, while eradicating bacterial biofilms is more challenging.[21] To observe the effect of PPNM-Gel on bacterial biofilm, the biofilm formed by *S. aureus* and *E. coli* was treated with PVA/SA-Gel and different PPNM-Gel. Compared with the control group, all treatment groups led to bacterial biofilm destruction (Figure S6); the PPNM-Gel destroyed bacterial biofilms more than PVA/SA-Gel (Figure 7F); PPNM10-Gel had the strongest ability to destroy bacterial biofilms, destroying 52.6% and 49.8% of the bacterial biofilms of *S. aureus* and *E. coli,* respectively (Figure 7F). In the above in vitro antibacterial experiments, the antibacterial activity of PPNM-Gel first increased and then decreased with the increase of PPNM content. This might be related to the following factors: For PPNM-Gel with low PPNM content (PPNM5-Gel and PPNM10-Gel), antibacterial related activities, including POD-like and OXD-like activities, played a major role in the multienzyme-like activity, so the antibacterial performance of PPNM-Gel increased with the increase of PPNM content; However, for PPNM15-Gel and PPNM25-Gel, due to the increase of PPNM content, H_2O_2 produced by POD-like activity would quickly encounter PPNM and be converted into O_2 through CAT-like activity, reducing the ROS content, so the high PPNM content might inhibit ROS-mediated bacterial oxidative damage.

Healing of Bacterial-Infected Diabetic Wounds in vivo

Based on the antibacterial ability of PPNM-Gel obtained in vitro, STZ-induced diabetic SD rats were used to investigate whether they had the ability to promote the healing of bacterial-infected diabetic wounds in vivo. The type 2 diabetic rat model was established by injecting STZ. A full-thickness excised wound with 7 mm diameter was made on the back of each rat and was infected with *S. aureus* and *E. coli* suspension. The macroscopic changes of wounds in different groups of bacterial-infected diabetic model rats at all time points (0th, 3th, 6th, 9th and 12th day) were exhibited in Figure 8A. On the 3th day, the wound area of the control group was larger than those of the five treatment groups (Figure 8B and C), because the hydrogel could effectively remove necrotic tissue and destroy bacteria in the inflammatory phase, creating basic conditions for tissue repair and regeneration. On the 6th day, the wound area of the control group was still the largest, whereas the wound area of five treatment groups was significantly different, in which the wound repair area of PVA/SA-Gel group was obviously lower than those of different PPNM-Gel groups. The wound repair areas of the treatment groups were 44.6% for PVA/SA-Gel, 68.7% for PPNM5-Gel, 75.5% for PPNM10-Gel, 65.4% for PPNM15-Gel, and 61.6% for PPNM25-Gel, respectively. On the 9th day, the wound healing of the treatment groups was significantly better than that of the control group, and the wound repair areas of PPNM-Gel groups greater than 86.6%. On the 12th day, the wound areas of the control group and PVA/SA-Gel group were 22.2% and 11.5%, whereas the wound contraction of PPNM-Gel groups was basically completed, and the wound repair area of PPNM10-Gel group was as high as 98.0%. In a word, PPNM-Gel effectively promoted the healing of bacterial-infected diabetic wounds, especially in the mid stage of wound healing. This result may be correlated with the capacity of PPNM-Gel to effectively absorb wound exudates and eliminate pathogenic bacteria infection, thus leading to the reduction of inflammatory reaction in the wound area. Besides, the healing rate of infected wounds first increased and then decreased with the increase of PPNM content. Similar to the antibacterial effect in vitro, the antibacterial activity of PPNM-Gel with high PPNM content (PPNM25-Gel) was weaker than that with low PPNM content (PPNM10-Gel), and the residual bacteria would cause immune response and inflammation, thus delaying the regeneration of wound tissue. Meanwhile, high PPNM content might excessively clear ROS, leading to downregulation of VEGF expression and reduced angiogenesis.[47] Therefore, the healing rate of PPNM10-Gel was the fastest, higher than that of PPNM25-Gel.

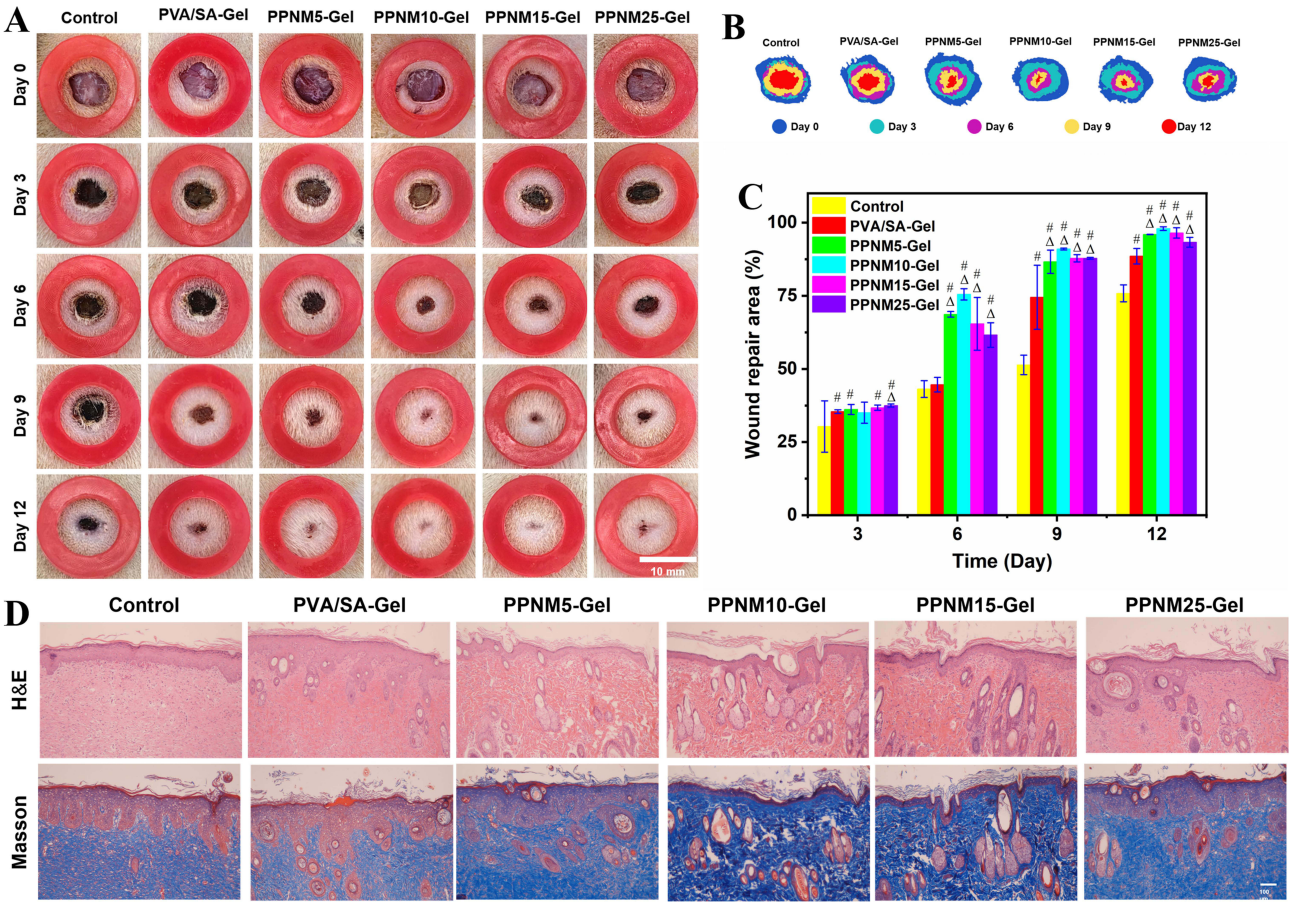

Figure 8 (**A**) Sample pictures show the bacterial-infected diabetic wounds of various treatments on different days, bar = 10 mm. (**B**) Traces of wound healing in different groups. (**C**) Change in wound repair area of different groups on different days ($^{\#}$Denotes $P < 0.05$ compared with the control group; $^{\Delta}$ Denotes $P < 0.05$ compared with the PVA/SA-Gel). (**D**) H&E and Masson staining of bacterial infected diabetic wound with different treatments, bar = 100 μm.

Wound healing is a highly complex biological process in the body, which can be divided into four chronologically sequential and overlapping phases: hemostasis, inflammation, proliferation (granulation), and remodeling.[48] On the 12th day after treatment, staining was applied to characterize the degree of wound re-epithelialization and the extent of collagen deposition histologically. H&E staining (Figure 8D) exhibited that the boundary between the epidermis and dermis was clearly defined and the redundant inflammatory cells still infiltrated the infected wound tissues. However, the thickness of the stratum corneum in the PPNM-Gel treated groups was significantly lower than that in the other groups, indicating that the wound healing process was in a later stage. In addition, the histological morphology of the PPNM-Gel treated wounds was sufficiently reconstructed, and many new sebaceous glands, hair follicles, and other cutaneous appendages were observed. Collagen deposition is one of the important features of wound healing, which is beneficial for the reconstruction of skin tissue arrangement.[2] Therefore, Masson staining was used to analyze collagen deposition. Similar to the H&E staining results, the amounts of collagen deposition in the control and PVA/SA-Gel groups were significantly lower than those in the PPNM-Gel treated groups. These results confirmed that the PPNM-Gel adequately accelerated the healing of bacterial-infected diabetic wounds by reconstructing histological structures and accumulating collagen fibers.

Bacterial-infected diabetic wounds are in inflammatory state due to the continuous release of a variety of inflammatory factors, which will trigger a chain reaction in the body. This cascade disrupts neovascularization, hampers cell proliferation, and thus hinders progress towards the proliferative stage, which is the main factor contributing to slow wound healing.[49,50] Ultimately, immunofluorescence assay was used to detect the expression level of inflammatory factors in wound tissue (Figure 9A–C). The expression levels of TNF-α (a pro-inflammatory factor) at the wound sites of

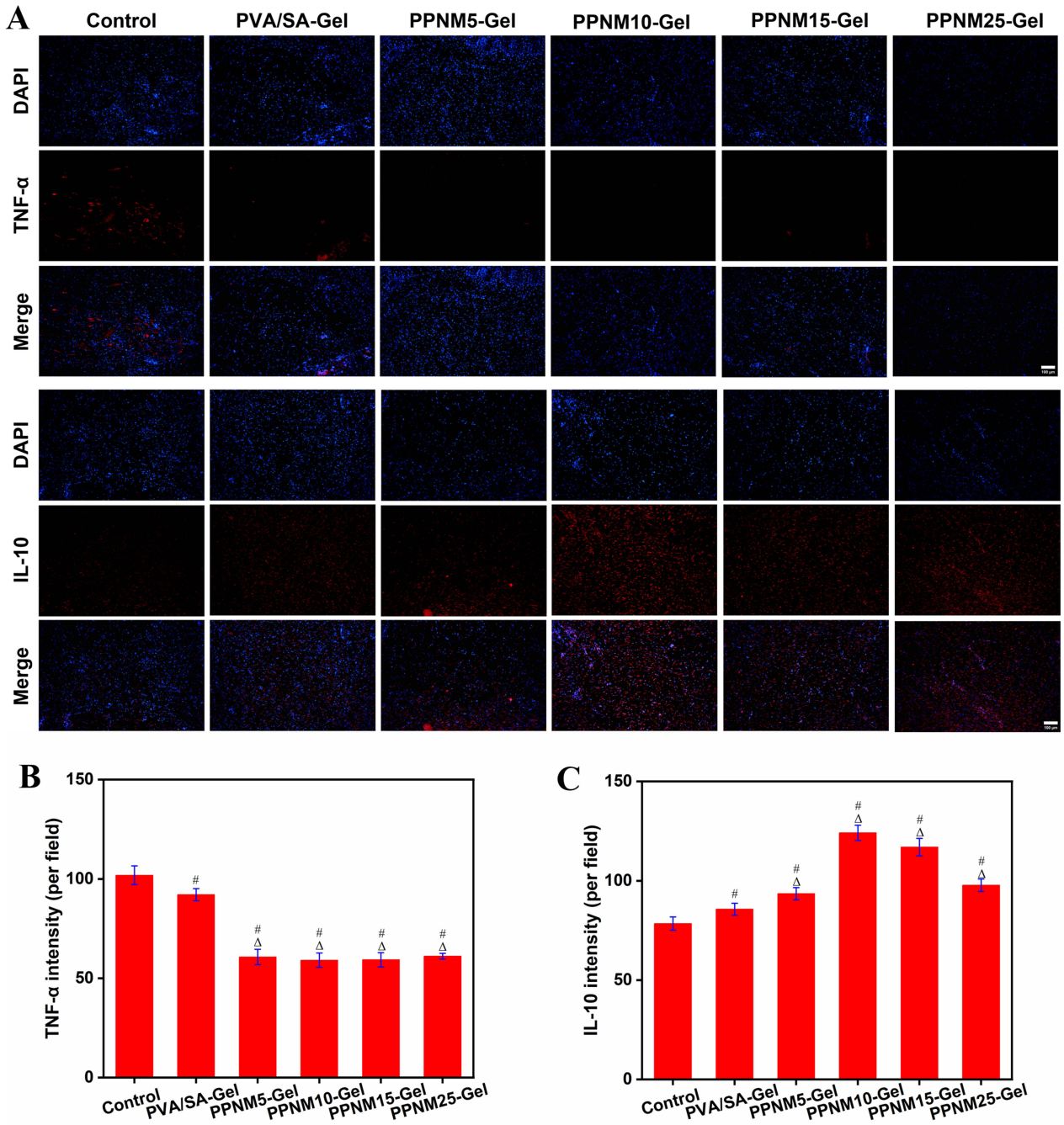

Figure 9 (**A**) Immunofluorescence images the expression of pro-inflammatory cytokine TNF-α and anti-inflammatory cytokine IL-10, bar = 100 μm. (**B** and **C**) Mean fluorescence density per field of view for TNF-α (**B**) and IL-10 (**C**) ($^{\#}$Denotes $P < 0.05$ compared with the control group; $^{\Delta}$Denotes $P < 0.05$ compared with the PVA/SA-Gel).

the PPNM-Gel treated groups were significantly lower than those of the control group and PVA/SA-Gel group (Figure 9B). In contrast, the expression levels of IL-10 (an anti-inflammatory factor) at the wound sites of the PPNM-Gel treated groups were significantly higher than those of the control group and PVA/SA-Gel group (Figure 9C). These results indicated that PPNM-Gel accelerated wound healing by regulating the inflammatory response at the wound site of bacterial infection. Among the PPNM-Gel treated groups, the PPNM10-Gel group exhibited the lowest TNF-α level and the highest IL-10 level, which demonstrated that the anti-inflammatory effect of PPNM10-Gel was the highest. During the healing of bacterial-infected diabetic wounds, the generation of RSO was beneficial for antibacterial activity and the

https://doi.org/10.2147/IJN.S540126

clearance of RSO was beneficial for alleviating oxidative stress. PPNM-Gel might exhibit corresponding enzyme activity based on the actual situation encountered. When encountering bacteria at the wound site, PPNM-Gel could quickly achieve antibacterial effects through OXD-like, POD-like, SOD-like, and NAD-like activities. Possible mechanisms include: H_2O_2 produced by bacteria in wounds was converted to •OH through the POD-like activity of PPNM; O_2 in the air was converted into •OH through the continuous catalysis of OXD-like, SOD-like, and POD-like activities of PPNM; The produced ROS could kill bacteria by ROS-mediated bacterial oxidative damage; In addition, the NAD-like activity of PPNM might partially block ATP synthesis and produce antibacterial effects. The ROS leaked from the wound in the later stage and the ROS produced by PPNM would cause the local ROS concentration in the wound to be too high. When encountering the high concentration ROS, PPNM might complete ROS-scavenging through CTA-like and SOD-like activities, promoting wound healing.

Conclusion

In summary, we developed an innovative trimetallic-doped PPNM with intrinsic multienzyme activity including POD-like, OXD-like, CAT-like, SOD-like, and NAD-like activities. Subsequently, the PPNM was anchored to PVA/SA matrix to construct PPNM-Gel as a wound dressing for accelerating the healing of bacterial-infected diabetic wounds. The wound healing mediated by PPNM-Gel might mainly involve the following three aspects: 1) When bacteria were present on the surface of the wound, PPNM-Gel could generate ROS through the OXD-like, SOD-like and POD-like activities to kill the bacteria; 2) Due to the excellent water absorption ability and tissue adhesive activity, PPNM-Gel could effectively adhere to the wound and absorb considerable inflammatory substances exuded from the wound; 3) Based on the CAT-like and SOD-like activities, PPNM-Gel could inhibit the elevated concentration of ROS associated with the inflammatory stage, thereby promoting wound healing. Compared with other nanozymes, PPNM had the advantages of easy preparation, low cost, and scalability, demonstrating a wide range of application prospects. However, our research had certain limitations, such as the lack of toxicity data for long-term PPNM exposure, poor adhesion of PPNM-Gel in dynamic wound environments, and the unclear mechanism by which PPNM regulates the generation and clearance of RSO. Future research will address the above limitations and use PPNM-Gel to treat other diseases affected by bacterial infections and high ROS levels.

Ethics Approval and Consent

Animal experiments were approved by the Institutional Animal Care and Use Committee of Chinese PLA General Hospital (No. SQ2023657) and strictly followed with the Guide for the Care and Use of Laboratory Animals of China.

Acknowledgments

This work has not received funding.

Disclosure

The authors declare that they have no conflicts of interest.

References

1. Martin P, Pardo-Pastor C, Jenkins RG, Rosenblatt J. Imperfect wound healing sets the stage for chronic diseases. *Science*. 2024;386(6726):eadp2974. doi:10.1126/science.adp2974
2. Wei YJ, Chen H, Zhou ZW, et al. Kill two birds with one stone: dual-metal mof-nanozyme-decorated hydrogels with ROS-scavenging, oxygen-generating, and antibacterial abilities for accelerating infected diabetic wound healing. *Small*. 2024;20(48):2403679. doi:10.1002/smll.202403679
3. John JV, Sharma NS, Tang G, et al. Nanofiber aerogels with precision macrochannels and LL-37-mimic peptides synergistically promote diabetic wound healing. *Adv Funct Mater*. 2023;33(1):2206936. doi:10.1002/adfm.202206936
4. Jia Z, Gong J, Zeng Y, et al. Bioinspired conductive silk microfiber integrated bioelectronic for diagnosis and wound healing in diabetes. *Adv Funct Mater*. 2021;31(19):2010461. doi:10.1002/adfm.202010461
5. Wang P, Wu J, Yang H, et al. Intelligent microneedle patch with prolonged local release of hydrogen and magnesium ions for diabetic wound healing. *Bioact Mater*. 2023;24:463–476. doi:10.1016/j.bioactmat.2023.01.001
6. Wang S, Zhang Y, Sun F, et al. Catalase-like nanozymes combined with hydrogel to facilitate wound healing by improving the microenvironment of diabetic ulcers. *Mater Design*. 2023;225:111557. doi:10.1016/j.matdes.2022.111557
7. Sharma S, Schaper N, Rayman G. Microangiopathy: is it relevant to wound healing in diabetic foot disease? *Diabetes-Metab Res Rev*. 2020;36(S1):e3244. doi:10.1002/dmrr.3244

8. Wei S, Xu P, Yao Z, et al. A composite hydrogel with co-delivery of antimicrobial peptides and platelet-rich plasma to enhance healing of infected wounds in diabetes. *Acta Biomater*. 2021;124:205–218. doi:10.1016/j.actbio.2021.01.046
9. Mirhaj M, Labbaf S, Tavakoli M, Seifalian AM. Emerging treatment strategies in wound care. *Int Wound J*. 2022;19(7):1934–1954. doi:10.1111/iwj.13786
10. Gong J, Wang H, Xie C, Dai Y, Wang Y, Guo W. A multifunctional injectable hydrogel for boosted diabetic wound healing assisted by Quercetin-ZIF system. *Chem Eng J*. 2024;495:153425. doi:10.1016/j.cej.2024.153425
11. Zhang R, Jiang B, Fan K, Gao L, Yan X. Designing nanozymes for in vivo applications. *Nat Rev Bioeng*. 2024;2(10):849–868. doi:10.1038/s44222-024-00205-1
12. Zandieh M, Liu J. Nanozymes: definition, activity, and mechanisms. *Adv Mater*. 2024;36(10):2211041. doi:10.1002/adma.202211041
13. Mei L, Zhu S, Liu Y, Yin W, Gu Z, Zhao Y. An overview of the use of nanozymes in antibacterial applications. *Chem Eng J*. 2021;418:129431. doi:10.1016/j.cej.2021.129431
14. Singh N, Savanur MA, Srivastava S, D'Silva P, Mugesh G. A redox modulatory Mn_3O_4 nanozyme with multi-enzyme activity provides efficient cytoprotection to human cells in a Parkinson's disease model. *Angew Chem Int Ed*. 2017;56(45):14267–14271. doi:10.1002/anie.201708573
15. Wen Y, Chen W, Wu R, et al. Chitosan-stabilized PtAu nanoparticles with multienzyme-like activity for mixed bacteria infection wound healing and insights into its antibacterial mechanism. *Small Struct*. 2024;5(6):2300553. doi:10.1002/sstr.202300553
16. Chen L, Wang X, Ren M, et al. Promoting the healing of infected diabetic wound by nanozyme-containing hydrogel with anti-bacterial inflammation suppressing, ROS-scavenging and oxygen-generating properties. *J Biomed Mater Res*. 2024;112(8):e35458. doi:10.1002/jbm.b.35458
17. Tu C, Lu H, Zhou T, et al. Promoting the healing of infected diabetic wound by an anti-bacterial and nano-enzyme-containing hydrogel with inflammation-suppressing, ROS-scavenging, oxygen and nitric oxide-generating properties. *Biomaterials*. 2022;286:121597. doi:10.1016/j.biomaterials.2022.121597
18. Yan X, Zheng W, Yu Y, et al. Dextran-functionalized cerium oxide nanoparticles for treating diabetic wound infections by synergy between antibacterial activity and immune modulation. *Mater Today Bio*. 2025;33:101977. doi:10.1016/j.mtbio.2025.101977
19. Jin HG, Zhao PC, Qian Y, Xiao JD, Chao ZS, Jiang HL. Metal-organic frameworks for organic transformations by photocatalysis and photothermal catalysis. *Chem Soc Rev*. 2024;53(18):9378–9418. doi:10.1039/d4cs00095a
20. Lin C, Guo X, Chen L, You T, Lu J, Sun D. Ultrathin trimetallic metal–organic framework nanosheets for accelerating bacteria-infected wound healing. *J Colloid Interf Sci*. 2022;628:731–744. doi:10.1016/j.jcis.2022.08.073
21. Ren X, Chang L, Hu Y, et al. Au@MOFs used as peroxidase-like catalytic nanozyme for bacterial infected wound healing through bacterial membranes disruption and protein leakage promotion. *Mater Design*. 2023;229:111890. doi:10.1016/j.matdes.2023.111890
22. Dong R, Guo B. Smart wound dressings for wound healing. *Nano Today*. 2021;41:101290. doi:10.1016/j.nantod.2021.101290
23. Deng Y, Zheng J, Li J, et al. NIR light-driven nanomotor with cascade photodynamic therapy for MRSA biofilm eradication and diabetic wound healing. *Theranostics*. 2025;15(8):3474–3489. doi:10.7150/thno.109356
24. Zhang Z, Ding Y, Yuan H, et al. A multiple-crosslinked injectable hydrogel for modulating tissue microenvironment and accelerating infected diabetic wound repair. *J Nanobiotechnol*. 2025;23(1):218. doi:10.1186/s12951-025-03285-2
25. Yang F, Mo D, Wu B, et al. Photo-controlled multifunctional hydrogel for photothermal sterilization and microenvironment amelioration of infected diabetic wounds. *J Control Release*. 2025;377:470–484. doi:10.1016/j.jconrel.2024.11.047
26. Ma H, Luo Y, Wang Y, et al. Artificial multienzyme nanoflower composite hydrogel for efficiently promoting MRSA-infected diabetic wound healing via glucose-activated NO releasing and microenvironment regulation. *Bioact Mater*. 2025;49:531–548. doi:10.1016/j.bioactmat.2025.03.014
27. Xie H, Tian S, Cui C, et al. A glycopeptide-based pH-responsive hydrogel promotes diabetic wound healing via antimicrobial and remodeling microenvironment. *Colloids Surf B*. 2025;251:114614. doi:10.1016/j.colsurfb.2025.114614
28. Chu Z, Liu X, Zhao T, et al. Self-healing Ppy-hydrogel promotes diabetic skin wound healing through enhanced sterilization and macrophage orchestration triggered by NIR. *Biomaterials*. 2025;315:122964. doi:10.1016/j.biomaterials.2024.122964
29. Meng H, Zhao Y, Cai H, et al. Hydrogels containing chitosan-modified gold nanoparticles show significant efficacy in healing diabetic wounds infected with antibiotic-resistant bacteria. *Int J Nanomed*. 2024;19:1539–1556. doi:10.2147/IJN.S448282
30. Li Q, Dong M, Han Q, et al. Enhancing diabetic wound healing with a pH-responsive nanozyme hydrogel featuring multi-enzyme-like activities and oxygen self-supply. *J Control Release*. 2024;365:905–918. doi:10.1016/j.jconrel.2023.12.015
31. Yuan J, Duan H, Wang L, Wang S, Li Y, Lin J. A three-in-one hybrid nanozyme for sensitive colorimetric biosensing of pathogens. *Food Chem*. 2023;408:135212. doi:10.1016/j.foodchem.2022.135212
32. Wang Y, Shi HD, Zhang HL, et al. A multifunctional nanozyme with NADH dehydrogenase-like activity and nitric oxide release under near-infrared light irradiation as an efficient therapeutic for antimicrobial resistance infection and wound healing. *Adv Healthcare Mater*. 2023;12(25):2300568. doi:10.1002/adhm.202300568
33. Jiang C, Sun M, Wang Y, et al. Coordination engineering in Fe-Mn dual-atom nanozyme: yielding ROS storm to efficiently promote wound healing. *Adv Funct Mater*. 2025;2424599. doi:10.1002/adfm.202424599
34. Tan X, Lin N, Yang S, et al. AuCu@CuO_2 aerogels with H_2O_2/O_2 self-supplying and quadruple enzyme-kike activity for MRSA-infected diabetic wound management. *Adv Sci*. 2025;12(27):2502391. doi:10.1002/advs.202502391
35. Xue Y, Liu K, Gao M, et al. Vancomycin-stabilized platinum nanoparticles with oxidase-like activity for sensitive dopamine detection. *Biomolecules*. 2023;13(9):1312. doi:10.3390/biom13091312
36. Cao S, Zhao Z, Zheng Y, et al. A library of ROS-catalytic metalloenzyme mimics with atomic metal centers. *Adv Mater*. 2022;34(16):2200255. doi:10.1002/adma.202200255
37. Lu W, Chen J, Kong L, Zhu F, Feng Z, Zhan J. Oxygen vacancies modulation Mn_3O_4 nanozyme with enhanced oxidase-mimicking performance for L-cysteine detection. *Sens Actuator B Chem*. 2021;333:129560. doi:10.1016/j.snb.2021.129560
38. Nana L, Ruiyi L, Qinsheng W, et al. Colorimetric detection of chlorpyrifos in peach based on cobalt-graphene nanohybrid with excellent oxidase-like activity and reusability. *J Hazard Mater*. 2021;415:125752. doi:10.1016/j.jhazmat.2021.125752
39. Wang Y, Bu T, Cao Y, et al. A versatile PdRu bimetallic nanoenzyme-integrated enzyme-linked immunosorbent assay for highly sensitive *Escherichia coli* O157:H7 detection. *Analy Chem*. 2023;95(24):9237–9243. doi:10.1021/acs.analchem.3c00743
40. Duan W, Wang J, Peng X, et al. Rational design of trimetallic AgPt–Fe_3O_4 nanozyme for catalyst poisoning-mediated CO colorimetric detection. *Biosens Bioelectron*. 2023;223:115022. doi:10.1016/j.bios.2022.115022

41. Wu SC, Tsai TT, Li TH, et al. Palladium-platinum bimetallic nanomaterials and their application in Staphylococcus aureus detection on paper-based devices. *Biosens Bioelectron*. 2022;216:114669. doi:10.1016/j.bios.2022.114669
42. Liu C, Zhao X, Wang Z, et al. Metal-organic framework-modulated Fe_3O_4 composite au nanoparticles for antibacterial wound healing via synergistic peroxidase-like nanozymatic catalysis. *J Nanobiotechnol*. 2023;21(1):427. doi:10.1186/s12951-023-02186-6
43. Zhang J, Bai Q, Bi X, et al. Piezoelectric enhanced peroxidase-like activity of metal-free sulfur doped graphdiyne nanosheets for efficient water pollutant degradation and bacterial disinfection. *Nano Today*. 2022;43:101429. doi:10.1016/j.nantod.2022.101429
44. Zhao X, Chang L, Hu Y, et al. Preparation of photocatalytic and antibacterial mof nanozyme used for infected diabetic wound healing. *ACS Appl Mater Interfaces*. 2022;14(16):18194–18208. doi:10.1021/acsami.2c03001
45. Pang Q, Jiang Z, Wu K, Hou R, Zhu Y. Nanomaterials-based wound dressing for advanced management of infected wound. *Antibiotics*. 2023;12(2):351. doi:10.3390/antibiotics12020351
46. Xue Y, Zhang L, Liu F, et al. Alkaline "Nanoswords" coordinate ferroptosis-like bacterial death for antibiosis and osseointegration. *ACS Nano*. 2023;17(3):2711–2724. doi:10.1021/acsnano.2c10960
47. Zhang S, Xu R, He S, et al. Nanozyme-driven multifunctional dressings: moving beyond enzyme-like catalysis in chronic wound treatment. *Military Med Res*. 2025;12(1):27. doi:10.1186/s40779-025-00611-5
48. Li Y, Zhu Z, Li S, et al. Exosomes: compositions, biogenesis, and mechanisms in diabetic wound healing. *J Nanobiotechnol*. 2024;22(1):398. doi:10.1186/s12951-024-02684-1
49. Zhu J, Zhou H, Gerhard EM, et al. Smart bioadhesives for wound healing and closure. *Bioact Mater*. 2023;19:360–375. doi:10.1016/j.bioactmat.2022.04.020
50. Kang X, Guan P, Xiao C, et al. Injectable intrinsic photothermal hydrogel bioadhesive with on-demand removability for wound closure and MRSA-infected wound healing. *Adv Healthcare Mater*. 2023;12(13):2203306. doi:10.1002/adhm.202203306